Effects of Strain Hardening and the Lode Dependence of the Fracture Strain Locus on Slant Fracture in Charpy V-Notch Impact Testing

Wong, Wei Jun; Walters, Carey L.

DOI
10.1115/OMAE2024-125635

Publication date
2024

Document Version
Final published version

Published in
Materials Technology; Subsea Technology

Proceedings of the ASME 2024 43rd International Conference on Ocean, Offshore and Arctic Engineering
OMAE2024
June 9-14, 2024, Singapore, Singapore

OMAE2024-125635

EFFECTS OF STRAIN HARDENING AND THE LODE DEPENDENCE OF THE FRACTURE STRAIN LOCUS ON SLANT FRACTURE IN CHARPY V-NOTCH IMPACT TESTING

Wei Jun Wong*, Carey L. Walters

Department of Maritime and Transport Technology
Delft University of Technology
Delft, The Netherlands

ABSTRACT

Ductile fracture in steels relevant to the offshore and maritime industry is often characterized by the occurrence of slant fracture, which is the development of fracture surfaces that are slanted relative to the original surface of the material. The modeling of this phenomenon is important for describing ductility and fracture toughness accurately in ductile fracture simulations. This work uses a consistency model for viscoplasticity with damage softening within a strain-based framework to investigate the effect of variations in strain hardening and Lode dependence on the slant fracture area and impact energy in Charpy tests. The model is first calibrated to uniaxial tensile, single-edge-notched-bending fracture toughness and instrumented Charpy tests performed on an S690QL steel, and then a parametric study varying the strain hardening and the Lode-dependence is performed. It is seen that an increase in the yield-to-tensile-strength ratio (equivalent to a decrease in the strain hardening exponent) leads to a decrease in the impact energy and negligible difference in the percentage slant fracture area when the damage and rate parameters are kept constant. It is found that the Charpy impact energy is not sensitive to the maximum strains in the fracture strain locus and is mainly affected by the minimum strains in the locus. Finally, the rate-dependent consistency plasticity model with a strain-based damage-softening formulation is capable of simulating slant fracture behavior even in cases where the fracture initiation strain is stress-state-independent and constant.

Keywords: Shear lips, ductile fracture, viscoplasticity, consistency model

1. INTRODUCTION

Modeling the detailed ductile fracture of steel requires capturing the effect of slant fracture. This is a phenomenon whereby the fracture surface does not develop perpendicularly to the direction of the maximum principal stress, due to the accumulation of shear strains. It can be seen microscopically that slant fracture involves a markedly different mechanism from flat fracture, where slant fracture exhibits smaller dimples than flat fracture, which is taken to mean that void growth is limited [1]. This difference in mechanisms leads to practical implications. For example, the occurrence of slant fracture has been seen to be promoted by factors such as a lower strain hardenability [2], a higher loading rate [3] and a greater specimen thickness [2]. Hence, the modeling of this phenomenon is important for understanding and accurately describing ductility and fracture toughness in fracture simulations.

Although slant fracture behavior has been successfully simulated for cracked and uncracked quasi-static tests [4–6] and cracked dynamic tests [7, 8], modeling of the uncracked, dynamic Charpy test that captures both slant fracture and rate-dependence in the material behavior is not found in the literature, due to the associated modeling difficulties [9–11]. Numerical models of ductile Charpy tests considering rate-dependence but neglecting slant fracture are often used [10–15].

Hence, this paper shows how a consistency model for viscoplasticity with damage softening can be used to simulate slant fracture in Charpy tests. Then, the model is used to investigate the effect of variations in strain hardening and in the Lode dependence of the fracture strain locus on the Charpy impact energy C_v and the slant fracture area A_s in a parametric study.

Strain hardening here refers to the gradient of the plastic hardening stress $\bar{\sigma}$ (Section 2.1) with respect to the amount of plastic straining that has occurred. The normalized Lode angle $\bar{\theta}$ [16] is an invariant of the deviatoric stress tensor, i.e. the part of the stresses associated with shape or shearing changes isolated from volumetric changes, that describes deviatoric stress states ranging from axisymmetric tension ($\bar{\theta} = 1$) to isochoric or simple shear ($\bar{\theta} = 0$) to axisymmetric compression ($\bar{\theta} = -1$).

These two properties are chosen because they have been identified in the literature as key factors influencing switching between slant and flat fracture in simulations of quasi-static fracture

*Corresponding author: W.J.Wong@tudelft.nl

tests [17]. Furthermore, the strain hardenability is used by many rules and standards in the form of the yield-to-tensile-strength ratio (σ_y/σ_u) to indirectly impose a minimum ductility requirement due to its relation to necking [18, 19], but its influence on ductile fracture behavior which also affects a structure's attainable ductility is not well understood. Understanding any correlations between strain hardenability on ductile fracture behavior could help improve the understanding of the role of the yield-to-tensile-strength ratio as an indirect ductility indicator.

A brief description of the rate-dependent damage-softening plasticity model (Sect. 2) and its calibration (Sect. 3) is first given [1]. Then, the effect of strain hardening on C_v and the extent of slant fracture is studied in Sect. 4 by varying the yield-to-tensile strength ratio. Finally, the effect of the Lode-dependence of the fracture strain locus is studied in Sect. 5) by varying the damage parameters defining the strain-based fracture locus.

2. RATE-DEPENDENT DAMAGE-SOFTENING PLASTICITY MODEL

The material is described by an elasto-viscoplastic consistency model based on Wang and Sluys [20] that is coupled with the damage softening model of Li and Wierzbicki [21] and a modified form of the Cowper-Symonds [22] strain rate model. Von Mises yielding with the associated flow rule is assumed. The yield function is given by Eq. (1):

$$f = \sigma_v - \bar{\sigma} R \beta \tag{1}$$

where σ_v, $\bar{\sigma}$, R and β are the von Mises equivalent stress, the plastic strain-hardening stress (Sect. 2.1), the rate-dependence factor (Sect. 2.2) and the softening coefficient (Sect. 2.3), respectively. The return-mapping for the calculation of the stresses, plastic strain increments and plastic strain rates which satisfy the consistency condition ($f = \dot{f} = 0$) [20] are implemented using an Abaqus Explicit [23] VUMAT user subroutine.

2.1 Plastic strain hardening

A Hollomon-type [24] power-law hardening curve with a yield plateau is assumed for the quasi-static undamaged true plastic stress-strain curve defined below, as given by Eqs. (2) and (3):

$$\bar{\sigma} = \begin{cases} \sigma_y \left(\dfrac{\varepsilon_{sh} - \dfrac{\sigma_y}{E}}{\varepsilon_{sh,p}} \varepsilon_p + \dfrac{\sigma_y}{E} + 1 \right) & 0 < \varepsilon_p < \varepsilon_{sh,p} \\ K {\varepsilon_p}^n & \varepsilon_p > \varepsilon_{sh,p} \end{cases} \tag{2}$$

$$\varepsilon_{sh,p} = \ln(1 + \varepsilon_{sh}) - \ln\left(1 + \frac{\sigma_y}{E}\right) \tag{3}$$

where $\bar{\sigma}$ is the plastic strain hardening stress; ε_p is the true equivalent plastic strain; ε_{sh} and $\varepsilon_{sh,p}$ are respectively the total engineering strain and the true equivalent plastic strain corresponding to the end of the yield plateau; K is the strength coefficient; and n is the strain hardening exponent.

[1]The detailed development of the model will be made available in a research journal article, whose manuscript, entitled *'Damage mechanics model for correlating notch toughness in Charpy impact tests with fracture toughness in cracked static fracture tests'*, is undergoing internal review at the time of writing.

2.2 Plastic rate dependence

The rate-dependence factor R is given by a modified form of the Cowper-Symonds [22] model:

$$R = 1 - \left(\frac{\dot{\varepsilon}_{p,uni} + \dot{\varepsilon}_{p0}}{C} \right)^{\frac{1}{q}} + \left(\frac{\dot{\varepsilon}_p + \dot{\varepsilon}_{p0}}{C} \right)^{\frac{1}{q}} \tag{4}$$

where C, q, $\dot{\varepsilon}_p$, $\dot{\varepsilon}_{p,uni}$ and $\dot{\varepsilon}_{p0}$ are the Cowper-Symonds coefficient, the Cowper-Symonds exponent, the equivalent plastic strain rate, the quasi-static-uniaxial-testing equivalent plastic strain rate parameter and the equivalent plastic strain rate offset parameter, respectively. This modification to the Cowper-Symonds expression is introduced to give R a finite (instead of infinite) slope with respect to $\dot{\varepsilon}_p$ at $\dot{\varepsilon}_p = 0\,\mathrm{s}^{-1}$ and a value of 1 when $\dot{\varepsilon}_p = \dot{\varepsilon}_{p,uni}$.

$\dot{\varepsilon}_{p,uni}$ and $\dot{\varepsilon}_{p0}$ are here taken to be $0.0067\,\mathrm{s}^{-1}$, the standard uniaxial testing rate according to ISO 6892-1 [25]. The parameters $C = 16\,112.5\,\mathrm{s}^{-1}$ and $q = 6.4$ are found by performing a least squares fit of Eq. 4 to room-temperature strain-rate characterization data found in the literature for maritime high-tensile steel grades H36 and similar (nominal yield strengths of either 345 or 355 MPa), as shown in Fig. 1 [26–32].

The strain rates in the studies shown in Fig. 1 had been obtained using a range of different methods, such as using a high-speed-video extensometer on the specimen [32], a split-Hopkinson pressure bar (SHPB) with strain gages [30], a one-bar method similar in principle to the SHPB [28], or a nominal rate based on the loading speed [29]. In the cases where the strain rates are measured from strain gages or extensometers, an average strain rate was calculated over a chosen reference time interval, such as the measurement interval at yield or ultimate strength [28], the time period between yield and ultimate strength [30], or the entire test duration [32]. Although the difference in the measurement methods and calculation of the reported strain rate naturally gives rise to variations in the strain-rate data, a database spanning a large range of strain rates based on a consistent experimental procedure is not available in the literature. Hence, a best-fit average of the aggregate strain-rate data is adopted to give a rough estimate of the behavior.

It is also assumed that the strain-rate effect which is measured with respect to the longitudinal strain rate in the literature has the same effect with respect to the equivalent plastic strain rate $\dot{\varepsilon}_p$, based on the notion that the $\dot{\varepsilon}_p$ is defined so that it is equal to the longitudinal strain rate for the uniaxial tension of incompressible materials up to necking.

2.3 Damage softening

The softening coefficient β is a function of the build-up of damage given by the damage indicator D and the softening parameters m and D_c, according to Li and Wierzbicki [21]:

$$\beta = \begin{cases} 1 & D \leq 1 \\ \left(\dfrac{D_c - D}{D_c - 1} \right)^m & 1 < D < D_c \\ 0 & D = Dc \end{cases} \tag{5}$$

where m is the softening exponent which affects the rate of the degradation with respect to D, and D_c is the critical damage

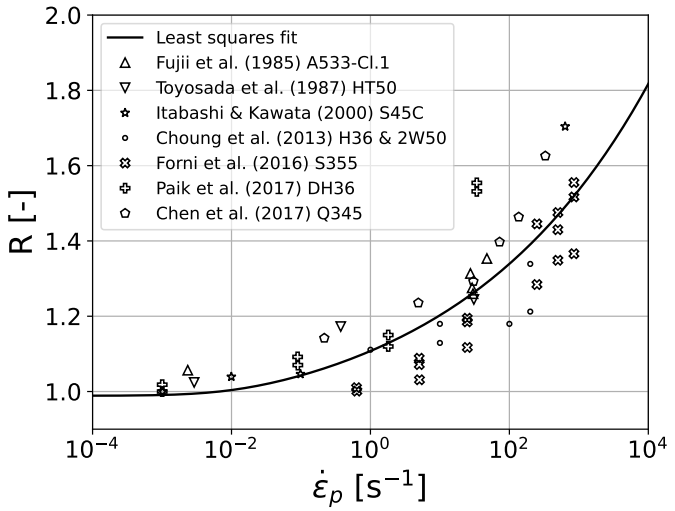

FIGURE 1: STRAIN-RATE DEPENDENCE OF THE PLASTIC FLOW STRESS BASED ON EXPERIMENTAL DATA [26–32].

corresponding to complete degradation (zero stress) and element deletion.

Damage is driven by the accumulation of plastic strains relative to the damage initiation strains ε_f, as shown in Eq. (6):

$$D = \int_0^{\varepsilon_p} \frac{1}{\varepsilon_f}\, d\varepsilon_p \tag{6}$$

where ε_f is given by the strain formulation of the Modified Mohr-Coulomb (MMC) [33] fracture surface:

$$\varepsilon_f = \left\{ \frac{K}{c_2}\left[c_3 + \frac{\sqrt{3}}{2-\sqrt{3}}(1-c_3)\left(\sec\frac{\bar{\theta}\pi}{6} - 1\right)\right] \times \left[\sqrt{\frac{1+{c_1}^2}{3}}\cos\frac{\bar{\theta}\pi}{6} + c_1\left(\eta + \frac{1}{3}\sin\frac{\bar{\theta}\pi}{6}\right)\right]\right\}^{-\frac{1}{n}} \tag{7}$$

where η is the stress triaxiality; $\bar{\theta}$ is the normalized Lode-angle; and c_1, c_2 and c_3 are the MMC strain parameters.

In the results below, the MMC strain parameters are expressed in normalized form for the ease of comparison during strain-based calibration and analysis, as shown in Eqs. (8) to (11):

$$C_1 = \left(\frac{c_2}{c_3 K Z}\right)^{\frac{1}{n}} \tag{8}$$

$$C_2 = \left(\frac{2c_2}{K}\right)^{\frac{1}{n}} \tag{9}$$

$$C_3 = \left(\frac{\sqrt{3}c_2}{K c_3}\right)^{\frac{1}{n}} \tag{10}$$

where Z is given by:

$$Z = \sqrt{\frac{1+{c_1}^2}{3}} + 2.5c_1 \tag{11}$$

These normalizations were chosen such that several special cases could be easily identified and independently controlled. Here, $C_1 = C_3$ corresponds to the triaxiality-independent ($c_1 = 0$) condition; C_2 and C_3 are the minimum and maximum strains in the strain surface for the triaxiality-independent case, respectively; and changing C_1 introduces triaxiality-dependence by adjusting the strain locus to pass through $\varepsilon_f = C_1$ at $\bar{\theta} = 0$ and $\eta = 2.5$, the linear plane-strain solution for the stress state in front of the crack tip [34].

A cut-off value of $-1/3$ for the negative triaxiality for fracture [35] is implemented by quadratically increasing ε_f to an arbitrarily large value the further η decreases below $-1/3$. For high triaxialities of $\eta > 3.5$, the ε_f is set to be constant based on the value of ε_f when $\eta = 3.5$. The relatively gradual nature of the ε_f increase around $\eta = -1/3$ and the constant ε_f past $\eta > 3.5$ are necessary for convergence in these η ranges during the stress update calculations, which assume that the variations in ε_f in time for a given element is relatively small (Eq. 12).

$$\frac{\delta D}{\delta \varepsilon_p} = \frac{1}{\varepsilon_f} \tag{12}$$

3. MODEL CALIBRATION

The model described in Sect. 2 involves 15 parameters as shown in Table 1. The parameters C, q, $\dot{\varepsilon}_{p,uni}$ and $\dot{\varepsilon}_{p0}$ are found as described in Sect. 2.2 above. The parameters E, ν, σ_y, $\varepsilon_{sh,p}$, K and n are derived from the pre-necking properties of the uniaxial tensile test. The parameters C_1, C_2, C_3, m and D_c are calibrated by iteratively identifying the values which simulate a close agreement in the experimental and simulated force-displacement responses of the tensile (Fig. 2), single-edge notched bending (SENB; Fig. 3) and Charpy (Fig. 4) tests simultaneously.

3.1 Experiments

The tests were performed on an S690QL [36] steel for the material direction transverse to the rolling direction. The plate had an original nominal thickness of 12 mm. The SENB fracture toughness test was performed at full thickness according to ASTM E1820 [37]. The tensile tests were performed according to ISO 6892-1 [25] on a 6-mm-thick half of the plate, in the form of a proportional flat tensile specimen with a 25-mm [38] width in the parallel length. An MTS-E22 Charpy testing machine with a pendulum mass of 32.85 kg, a pendulum energy of 450 J and a striking speed of 5234 mm s^{-1} was used for the instrumented Charpy tests performed according to the ISO standards [39, 40].

3.2 Calibrated finite-element simulations

The density ρ of steel was assumed to be 7850 kg m^{-3}, and the coefficient of friction between the steel and the external contact surfaces in the Charpy and SENB tests was assumed to be 0.15, except for the two SENB support rollers which were modeled as frictionless. All the simulated specimens were discretized using Abaqus's C3D8R elements, which are 8-noded hexahedral elements with reduced integration and hourglass control [23]. Triaxiality independence ($C_1 = C_3$; Section 2.3) was assumed and found to result in a good calibration for the simulations.

TABLE 1: MATERIAL PARAMETER VALUES FOR THE S690QL STEEL.

E [GPa]	v [-]	σ_y [MPa]	$\varepsilon_{sh,p}$ [-]	K [MPa]	n [-]	C_1 [-]	C_2 [-]	C_3 [-]	m [-]	D_c [-]	C [s^{-1}]	q [-]	$\dot{\varepsilon}_{p,uni}$ [s^{-1}]	$\dot{\varepsilon}_{p0}$ [s^{-1}]
213.4	0.3	841	0.0256	1109.3	0.0675	0.4	0.5	0.4	1	1.5	16112.5	6.4	0.0067	0.0067

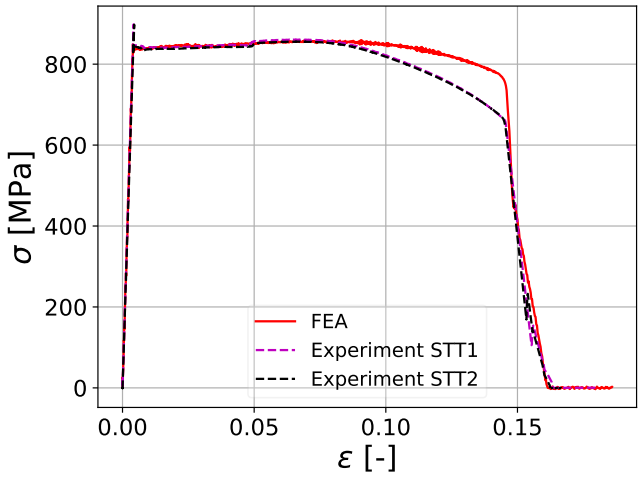

FIGURE 2: EXPERIMENTAL AND SIMULATED ENGINEERING STRESS-STRAIN CURVES.

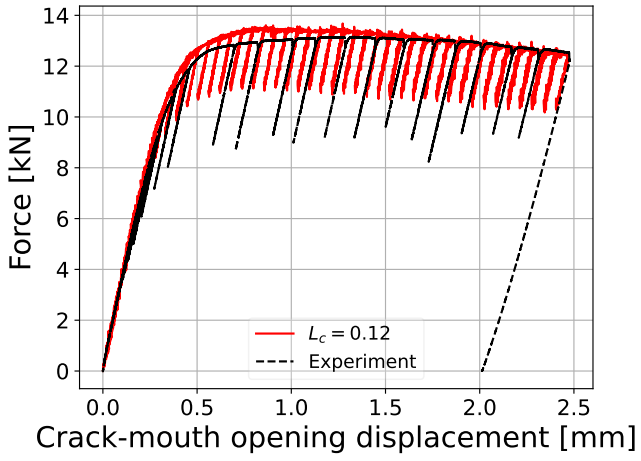

FIGURE 3: EXPERIMENTAL AND SIMULATED FORCE AGAINST CRACK-MOUTH OPENING DISPLACEMENT FOR THE SENB FRACTURE TOUGHNESS TEST.

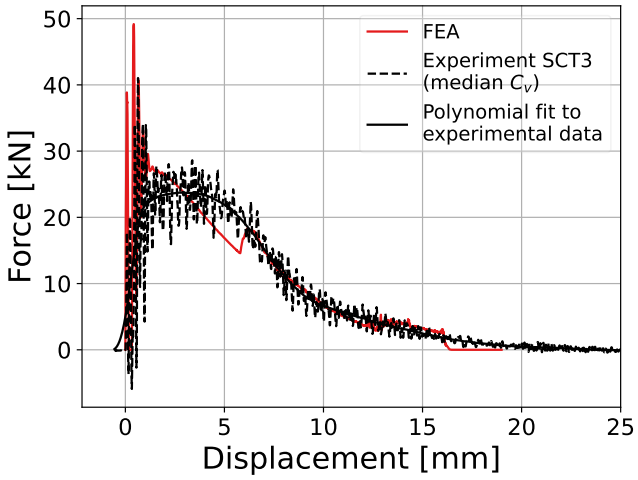

FIGURE 4: EXPERIMENTAL AND SIMULATED CHARPY IMPACT FORCE-DISPLACEMENT CURVES.

The calibrated parameters (Table 1) result in a relatively good agreement of the simulations with the experiments for the three tests simultaneously, which supports the validity of the modeling framework and the subsequent parametric findings. The tensile force-displacement curve (Fig. 2) captures the pre-necking behavior, the ultimate tensile stress and the fracture elongation to within 2 %, although a 15 % overestimation of the post-necking force in the tensile test is seen. The SENB force versus crack-mouth opening displacement curve (Fig. 3) shows good agreement in the overall curve but for a 4 % overestimation in the peak force.

The remainder of this paper focuses on the Charpy results. In the simulations, the striker and anvils were modeled as analytical rigid surfaces. The point on the tip of the striker that is aligned with the midspan and mid-thickness of the Charpy specimen was assigned with a half of the experimental pendulum mass, because a half model assuming symmetry about mid-thickness was used. The point mass was given an initial velocity of 5234 mm s^{-1}, as in the experiment, in a direction perpendicular to the undeformed Charpy specimen and restricted from displacement in any other degree of freedom other than that of the assigned velocity. The simulated Charpy impact energy, given by the loss in the kinetic energy of the point mass, is within 1 % of the mean of the impact energies of the three instrumented Charpy tests (Table 2).

The total contact force in the direction of the velocity due to contact pressure and frictional stress on the top surface of the specimen, multiplied by two to account for symmetry, is plotted against the displacement of the point mass for comparison against experimental results (Fig. 4) and also for the parametric studies further below. The initial oscillations in the force-displacement

TABLE 2: EXPERIMENTAL AND SIMULATED CHARPY IMPACT ENERGIES FROM THE INSTRUMENTED CHARPY TESTS.

	Experiments				FEA
	SCT1	SCT2	SCT3	mean	
C_v [J]	197.2	217.7	204.2	206.4	204.8

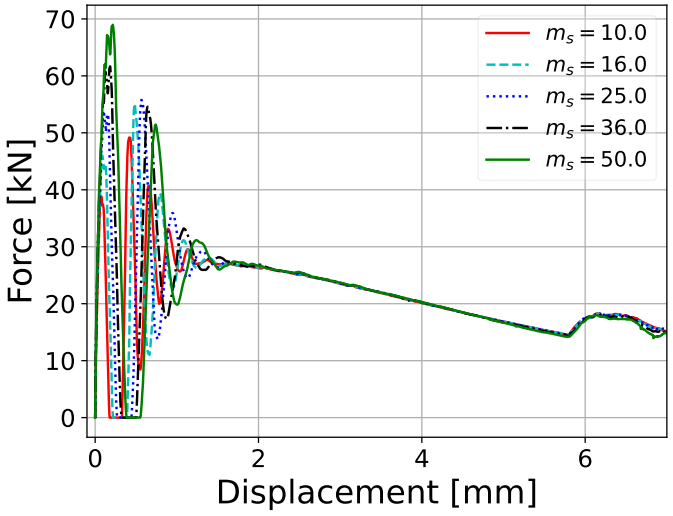

FIGURE 5: CHARPY SIMULATION RESULTS FOR DIFFERENT MASS SCALING FACTORS m_s.

record are due to dynamic effects. The overestimation of the simulated curve in this initial stage is attributed to the use of a mass scaling factor m_s, by which the mass in the finely meshed region around the notch (Fig. 6) is multiplied, to decrease the maximum stable time increment and speed up the analysis. The mass scaling factor is kept constant through the analysis. It can be seen in the mass scaling sensitivity study (Fig. 5 and Table 3) that mass scaling neither affects parts of the curve after the initial oscillations nor the C_v energy significantly. Based on this, the mass scaling factor of 10 was chosen for the Charpy simulation shown in Fig. 4 and also for the subsequent parametric studies in Sects. 4 and 5. The simulation results of the quasi-static tensile and SENB fracture toughness tests were far less sensitive to mass scaling, and extensive mass scaling was used for those simulations to speed up the computation time without any significant effects on the results and with the total kinetic energy staying less than 5 % of the total internal energy, except for the start of the analysis where the specimens first move before they deform.

The jump in the simulated force-displacement record at a displacement of around 6 mm could be attributed to the coarseness

TABLE 3: CHARPY IMPACT ENERGIES FOR DIFFERENT MASS SCALING FACTORS m_s.

	Simulations					Tests'
m_s [−]	50	36	25	16	10	mean
C_v [J]	209.3	209.0	207.3	204.7	204.8	206.4

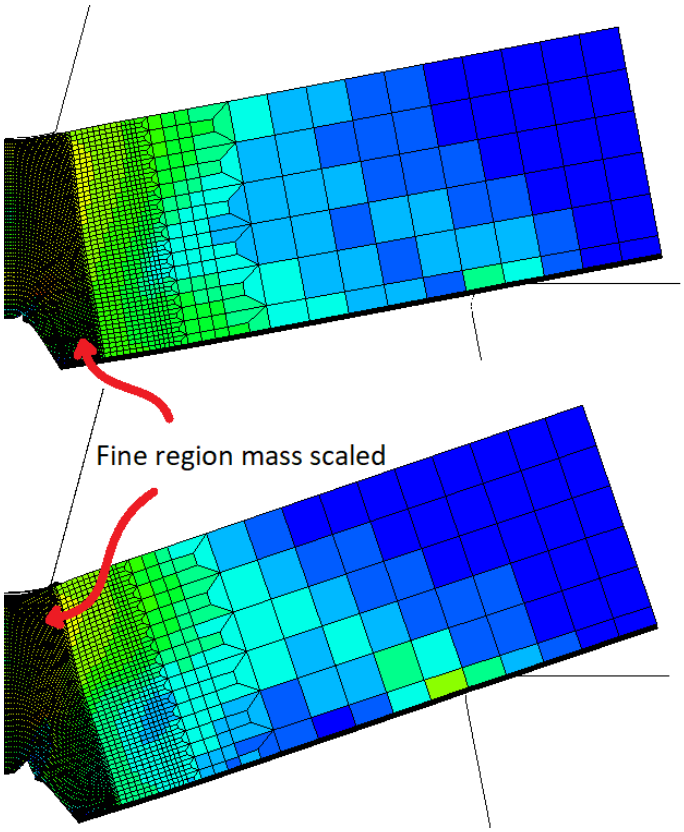

FIGURE 6: CONTOURS OF MISES STRESS SHOWING THE LOAD PATH CHANGING ITS COURSE TO PREDOMINANTLY PASS THROUGH A DIFFERENT NODE THAN BEFORE, SHORTENING THE SPAN.

of the mesh at the contact region at the supports. As the specimen rotates, the load path at the support changes its course from passing predominantly through one node to another, slightly changing the effective span (Fig. 6). It appears that a jump in the behavior is observed due to the relatively large element discretization in that zone and the linear formulation of the 8-noded hexahedral elements used. The shape of the curve could be improved by finer meshing; however, this artefact of discretization is not expected to significantly change the C_v or the overall behavior of the curve, and has hence been left as such in this study to save on computational costs.

A mesh sensitivity study was also performed to check whether the model was convergent with increasing mesh fineness. Local damage models such as the MMC [33] and GTN models [41] are subject to mesh sensitivity issues (non-convergence despite mesh refinement) [42]. The introduction of viscoplasticity, such as implemented in the present model (Sect. 2), is one of several approaches used to help reduce or eliminate mesh sensitivity [20], although not all approaches are always similarly effective in treating mesh sensitivity [43]. Fig. 7 shows the results of simulations in which the characteristic element size L_c of elements directly above the Charpy V-notch are varied per simulation, where L_c is here defined as the cube root of the volume of the element. From Fig. 7, the Charpy simulations do not appear to converge with mesh refinement, despite the underly-

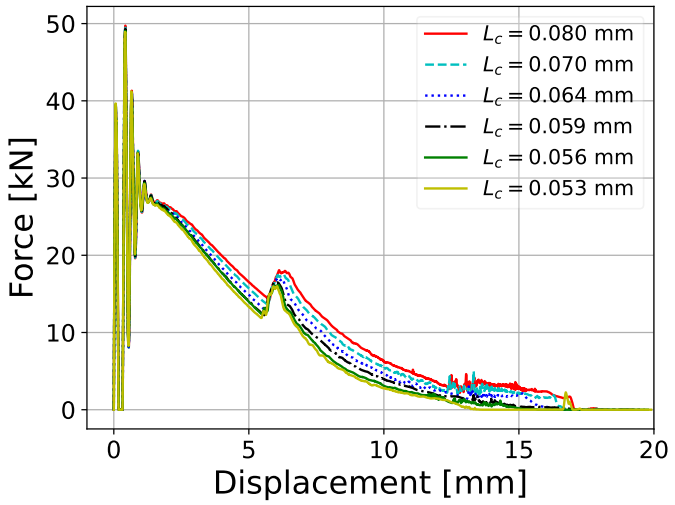

FIGURE 7: CHARPY SIMULATION RESULTS FOR DIFFERENT CHARACTERISTIC ELEMENT LENGTHS L_c.

ing viscoplastic formulation. Therefore, it must be noted that the present findings for the Charpy test are applicable to the chosen L_c of 0.08 mm. However, it is worth noting mesh convergence was observed in the mesh convergence studies for the the quasi-static tensile and SENB fracture toughness tests.

The simulated fracture morphology of the Charpy specimen captures the characteristic slant fracture surface observed in the tests (Fig. 8). In both the simulation and the experiment, the specimen has not been fully separated into two, although the crack has progressed further in the experiments than in the simulation. The observed asymmetry about the midspan plane is also stronger in the test, where the face shown in Fig. 8a sees the extensive development of one slanted crack face, while the simulated face in Fig. 8b sees the development of two slanted crack surfaces to different extents. This is difference is likely due to the material's inhomogeneity not being captured by the simulation, which assumed homogeneity in a half model with a symmetry plane at mid-thickness, such that the asymmetry in the modeled response occurred by virtue of floating-point inaccuracies.

4. EFFECT OF STRAIN HARDENING

Besides the strain hardening exponent n, the yield-to-tensile-strength ratio σ_y/σ_u obtained from the uniaxial tensile test can also be used to describe the strain hardenability, due to the relationship of these two properties given by Considère's [44] necking theory. The σ_y/σ_u ratio is often used because of the slightly greater ease of obtaining just σ_y and σ_u from tensile tests in comparison to calculating n from full stress-strain curves.

In this section, σ_y/σ_u is varied in a parametric study to investigate the effect of strain hardening on slant fracture and C_v, in the situation where the rate parameters and the strain-based damage parameters are held constant. The σ_y is kept constant based on the experimental value of 841 MPa from Sect. 3. The values of K and n are solved for by assuming that σ_u satisfies Considère's [44] criterion and that the Hollomon [24] power curve in Eq. 2 intersects with the yield plateau at a true plastic strain of $\varepsilon_p = \varepsilon_{sh,p} = 0.0256$, taken from the experiment above. All the other material parameters such as the calibrated damage parameters are kept constant.

Fig. 9 shows that an increase in the σ_y/σ_u leads to an decrease in C_v through an overall decrease in the force response in a Charpy test. It is seen that the peak force (ignoring the dynamic oscillations at the beginning) is decreased with increasing σ_y/σ_u, but the displacement at which the peak occurs, which corresponds to the start of element deletion ($D = D_c$), remains the same. The behavior described above can be expected due to the lower post-yield stresses that a lower σ_u entails and the strain-based nature of the framework, in which the onset of degradation is determined by achieving critical strains regardless of the stress.

It should be noted that how the damage parameters which describe the fracture strain locus are in general correlated to the yield-to-tensile strength ratio is not known. Nonetheless, this case study shows the capability of the established strain-based framework to study and quantify the effects of different factors on the ductile Charpy response in isolation while capturing the slant mechanism.

The effect of varying σ_y/σ_u in the simulations above on the extent of slant fracture that occurs was also investigated. The 2D-projected area (Fig. 10) of the crack face at the midspan of the Charpy specimen is used to find an indicator A_S of the extent of slant fracture, given by the slant fracture area taken as a percentage of the of total flat and slant fracture area. Fig. 10 shows the projected areas used for the calculations and the corresponding A_s for each simulation. Since slant fracture occurs on both faces (Fig. 8b), the face for which the slant fracture has progressed more is used. It is seen that varying σ_y/σ_u has little effect on the extent of slant fracture, with the A_s varying by at most 1 % over the range of $\sigma_y/\sigma_u = 0.82$ to 0.98, despite the higher σ_y/σ_u ratios of 0.94 and 0.98 (Figs. 10d and 10d) exhibiting a small amount of slant fracture occurring separately at the face top of the specimen, which is not a realistic prediction.

5. EFFECT OF LODE DEPENDENCE OF THE FRACTURE STRAIN LOCUS

The Lode dependence of the fracture strain locus is varied by varying the normalized damage parameters C_2 (Eq. (9)) and C_3 (Eq. (10)). In the present triaxiality independent case, C_2 equals to the maximum of the fracture strain locus, occurring at $\bar{\theta} = \pm 1$; and C_3 equals to the minimum of the fracture strain locus, occurring at $\bar{\theta} = 0$. Figs. 12 and 11 show that C_2 has a relatively small effect on C_v, and C_v is mostly dominated by C_3. This could be related to how tunneling starts at mid-thickness, and towards mid-thickness, $\bar{\theta}$ approaches 0, which corresponds to C_3. This suggests that the initial tunneling has a strong, determining influence on the subsequent overall response and the total C_v.

Finally, slant fracture like that in Fig. 8 was also seen in the four simulations in this parametric study involving a constant fracture strain ($\varepsilon_f = C_1 = C_2 = C_3$), where this constant ε_f was set in turn to 0.3, 0.4, 0.5 and 0.6. In the literature, Lode dependence has been identified as a key factor in the modeling of slant fracture [45]. The use of the present model reveals that it is possible to simulate slant fracture even with the assumption of a constant, triaxiality-independent and Lode-independent fracture initiation strain in a strain-based framework. In comparison with

(a) Experiment.

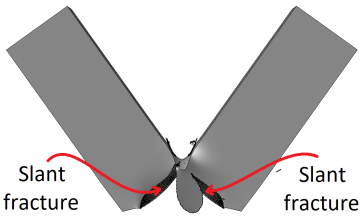

(b) Simulation.

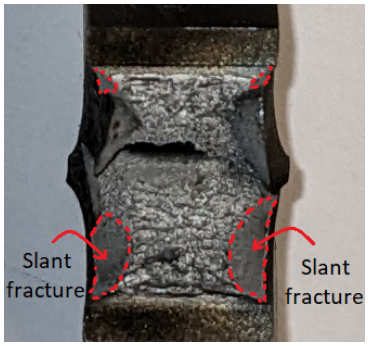

(c) Experiment.

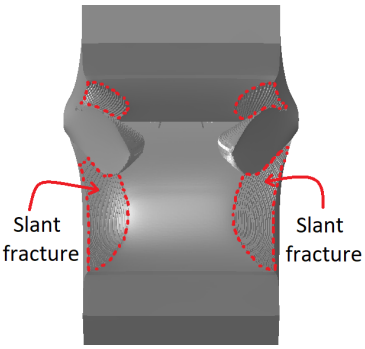

(d) Simulation.

FIGURE 8: EXPERIMENTAL (8a, 8c) AND SIMULATED (8b, 8d) FRACTURE MORPHOLOGIES IN THE CHARPY TEST.

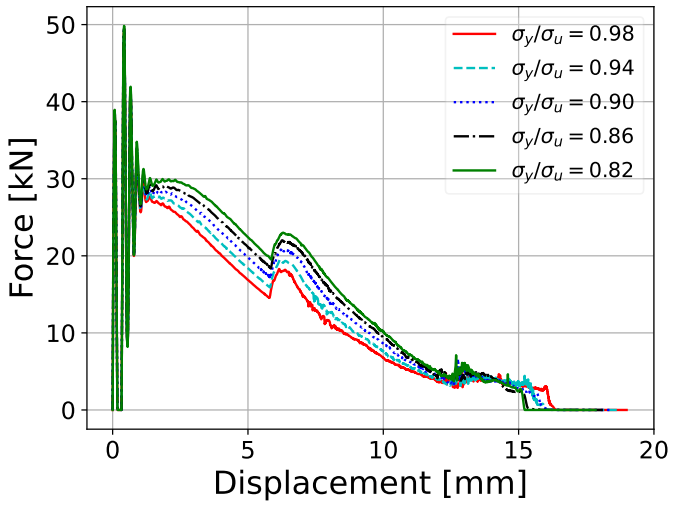

FIGURE 9: CHARPY SIMULATION RESULTS FOR DIFFERENT σ_y/σ_u RATIOS.

models formulated on a fracture stress criterion such as [46], the Lode dependence is here captured indirectly, since the stress at which the the fracture strain is achieved is not constant with respect to the Lode angle for the present model.

6. CONCLUSION

A rate-dependent consistency plasticity model with a strain-based damage-softening formulation has been used to simulate slant fracture in Charpy tests. The experimentally calibrated model was used for parametric case studies in which the strain hardening and the fracture strain locus were varied to observe the effects on the force-displacement response, Charpy impact energy and slant fracture area, demonstrating the capabilities of the model to capture and vary those effects in isolation. Finally, the strain-based damage model was shown to be capable of modeling slant fracture even with the assumption of a constant, stress-state-independent fracture initiation strain.

ACKNOWLEDGMENTS

The authors gratefully acknowledge the funding provided by the consortium of companies consisting of Bureau Veritas Marine & Offshore SAS, Damen Schelde Naval Shipbuilding BV, Huisman Equipment BV, Lloyd's Register EMEA, POSCO, as well as the Topconsortia voor Kennis en Innovatie (TKI). The authors thank Virginia Bertolo, Elise Reinton and Ton Riemslag of the Mechanical Behavior Lab of 3mE for lending and assisting with their experimental equipment and expertise.

REFERENCES

[1] Bron, Frédéric, Besson, Jacques and Pineau, André. "Ductile rupture in thin sheets of two grades of 2024

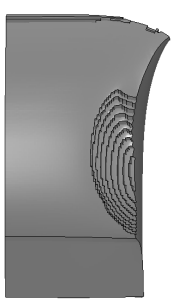

(a) σ_y/σ_u **= 0.82;** A_s = 16.5 %.

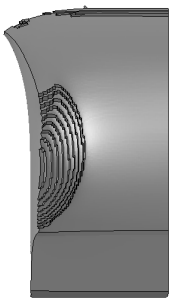

(b) σ_y/σ_u **= 0.86;** A_s = 16.9 %.

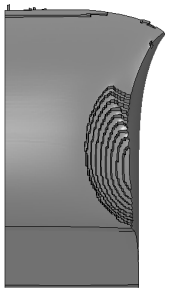

(c) σ_y/σ_u **= 0.90;** A_s = 16.8 %.

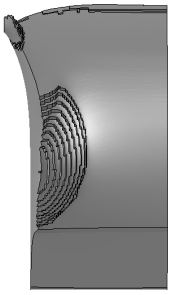

(d) σ_y/σ_u **= 0.94;** A_s = 17.0 %.

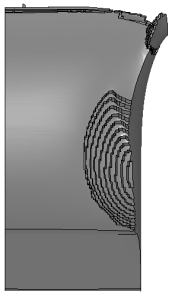

(e) σ_y/σ_u **= 0.98;** A_s = 17.5 %.

FIGURE 10: AREA OF SLANT FRACTURE SURFACE A_s FOR DIFFERENT σ_y/σ_u RATIOS.

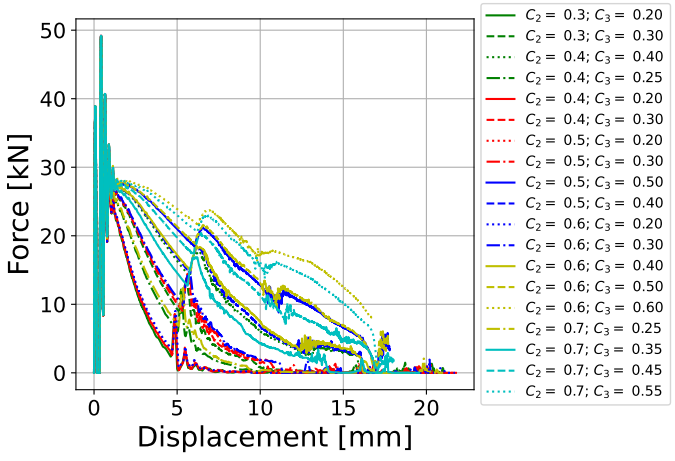

FIGURE 11: CHARPY SIMULATION RESULTS FOR DIFFERENT DIFFERENT C_2 AND C_3.

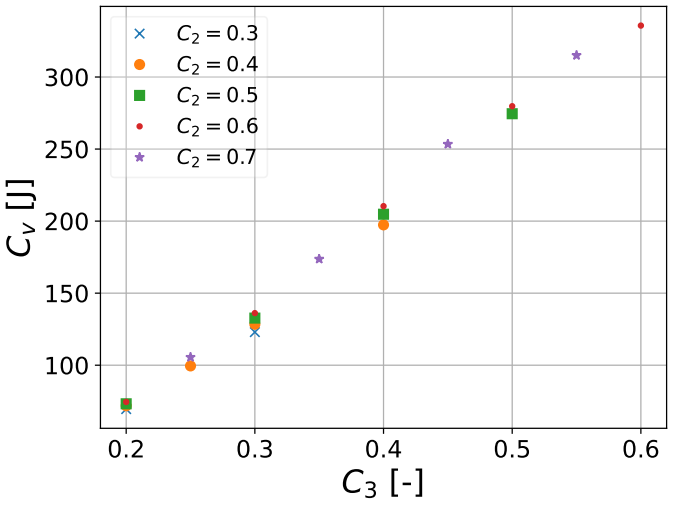

FIGURE 12: C_v AGAINST C_2 FOR DIFFERENT C_3.

aluminum alloy." *Materials Science and Engineering: A* Vol. 380 No. 1-2 (2004): pp. 356–364. DOI 10.1016/j.msea.2004.04.008.

[2] Asserin–Lebert, Alexandra, Besson, Jacques and Gourgues, Anne Francoise. "Fracture of 6056 aluminum sheet materials: effect of specimen thickness and hardening behavior on strain localization and toughness." *Materials Science and Engineering: A* Vol. 395 No. 1-2 (2005): pp. 186–194. DOI 10.1016/j.msea.2004.12.018.

[3] Rivalin, F., Pineau, André, Di Fant, Marc and Besson, Jacques. "Ductile tearing of pipeline-steel wide plates." *Engineering Fracture Mechanics* Vol. 68 No. 3 (2001): pp. 329–345. DOI 10.1016/s0013-7944(00)00107-7.

[4] Xue, Liang. "Damage accumulation and fracture initiation in uncracked ductile solids subject to triaxial loading." *International Journal of Solids and Structures* Vol. 44 No. 16 (2007): pp. 5163–5181. DOI 10.1016/j.ijsolstr.2006.12.026.

[5] Huang, Hongcheng and Xue, Liang. "Prediction of slant ductile fracture using damage plasticity theory." *International Journal of Pressure Vessels and Piping* Vol. 86 No. 5 (2009): pp. 319–328. DOI 10.1016/j.ijpvp.2008.11.027.

[6] Lan, Weiming, Deng, Xiaomin, Sutton, Michael A. and Cheng, Ching-Shan. "Study of slant fracture in ductile materials." *International Journal of Fracture* Vol. 141 No. 3-4 (2006): pp. 469–496. DOI 10.1007/s10704-006-9008-7.

[7] Novokshanov, Denis, Döbereiner, Benedikt, Sharaf, Mohamed, Münstermann, Sebastian and Lian, Junhe. "A new model for upper shelf impact toughness assessment with a computationally efficient parameter identification algorithm." *Engineering Fracture Mechanics* Vol. 148 (2015): pp. 281–303. DOI 10.1016/j.engfracmech.2015.07.069.

[8] Simha, C. Hari Manoj, Xu, Su and Tyson, William R. "Nonlocal phenomenological damage-mechanics-based modeling of the Drop-Weight Tear Test." *Engineering Fracture Mechanics* Vol. 118 (2014): pp. 66–82. DOI 10.1016/j.engfracmech.2014.01.009.

[9] Thibaux, Philippe, Müller, Sébastien, Tanguy, Benoit and van den Abeele, Filip. "Ductile Fracture Characterization of an X70 Steel: Re-Interpretation of Classical Tests Using the Finite Element Technique." *2008 7th International Pipeline Conference*, Vol. 3. Conference proceedings: pp. 179–186. Calgary, Alberta, Canada, 2009. DOI 10.1115/IPC2008-64291.

[10] Tanguy, Benoît, Luu, Trung T., Perrin, Gilles, Pineau, André and Besson, Jacques. "Plastic and damage behaviour of a high strength X100 pipeline steel: Experiments and modelling." *International Journal of Pressure Vessels and Piping* Vol. 85 No. 5 (2008): pp. 322–335. DOI 10.1016/j.ijpvp.2007.11.001.

[11] Hure, Jeremy, Parrot, Aurore and Meunier, Sébastien. "Numerical prediction of the effect of irradiation on the Charpy Upper Shelf Energy of Reactor Pressure Vessel steels." *Journal of Nuclear Materials* Vol. 570 (2022). DOI 10.1016/j.jnucmat.2022.153956.

[12] Besson, Jacques, Luu, Trung T., Tanguy, Benoit and Pineau, André. "Anisotropic Plastic And Damage Behavior of a High Strength Pipeline Steel." *The Nineteenth International Offshore and Polar Engineering Conference*. Conference paper. Osaka, Japan, 2009.

[13] Banerjee, Arkadeb, Dhar, Sankar, Acharyya, Sanjib Kumar, Datta, Debasis and Nayak, Nityananda. "Determination of Johnson Cook material and failure model constants and numerical modelling of Charpy impact test of armour steel." *Materials Science and Engineering: A* Vol. 640 (2015): pp. 200–209. DOI 10.1016/j.msea.2015.05.073.

[14] Schmitt, Winfried, Varfolomeyev, Igor V. and Böhme, Wolfgang. "Modelling of the Charpy test as a basis for toughness evaluation." *European Structural Integrity Society* Vol. 30 (2002): pp. 45–56. DOI 10.1016/S1566-1369(02)80005-X.

[15] Madhusudhan, Dasari, Chand, Suresh, Ganesh, Sattineni and Saibhargavi, U. "Modeling and simulation of Charpy impact test of maraging steel 300 using Abaqus." *IOP Conference Series: Materials Science and Engineering* Vol. 330 (2018). DOI 10.1088/1757-899x/330/1/012013.

[16] Bai, Yuanli and Wierzbicki, Tomasz. "A new model of metal plasticity and fracture with pressure and Lode dependence." *International Journal of Plasticity* Vol. 24 No. 6 (2008): pp. 1071–1096. DOI 10.1016/j.ijplas.2007.09.004.

[17] Xue, Liang and Wierzbicki, Tomasz. "Numerical simulation of fracture mode transition in ductile plates." *International Journal of Solids and Structures* Vol. 46 No. 6 (2009): pp. 1423–1435. DOI 10.1016/j.ijsolstr.2008.11.009.

[18] Feldmann, Markus, Schaffrath, Simon and Sandro, Citarelli. "Draft: Background document to Eurocode 3 EN 1993 – Part 1-10: Material toughness - Approach for upper-shelf toughness requirements for the design of steel structures based on damage mechanics." Report. Institute of Steel Construction RWTH Aachen University. 2020.

[19] Wong, Wei Jun and Walters, Carey Leroy. "Failure modes and rules related to the yield-to-tensile strength ratio in steel structures." *ASME 2021 40th International Conference on Ocean, Offshore and Arctic Engineering (OMAE)*. Conference proceedings. June 21-30, 2021, Virtual, Online, 2021. ASME (The American Society of Mechanical Engineers). DOI doi.org/10.1115/OMAE2021-61995.

[20] Wang, Wei Min, Sluys, Lambertus J. and de Borst, René. "Viscoplasticity for instabilities due to strain softening and strain-rate softening." *International Journal for Numerical Methods in Engineering* Vol. 40 No. 20 (1997): pp. 3839–3864. DOI 10.1002/(sici)1097-0207(19971030)40:20<3839::Aid-nme245>3.0.Co;2-6.

[21] Li, Yaning and Wierzbicki, Tomasz. "Prediction of plane strain fracture of AHSS sheets with post-initiation softening." *International Journal of Solids and Structures* Vol. 47 No. 17 (2010): pp. 2316–2327. DOI 10.1016/j.ijsolstr.2010.04.028.

[22] Cowper, G. Richard and Symonds, Paul S. "Strain hardening and strain-rate effects in the impact loading of cantilever beams." Report no. 28. Office of Naval Research. 1957.

[23] DS Simulia (Dassault Systèmes Simulia). "ABAQUS 2022. Commercial Finite Element Software." (2022).

[24] Hollomon, John Herbert Jr. "Tensile Deformation." *Transactions of the Metallurgical Society of AIME* Vol. 162 (1945): pp. 268–290.

[25] ISO (International Organization for Standardization). *ISO 6892-1 Metallic materials - Tensile testing - Part 1: Method of test at room temperature*. ISO, Geneva (2019).

[26] Fujii, Eisuke, Ohkuma, Isamu, Kawaguchi, Yoshiaki and Tsukamoto, Masatoshi. "Effects of temperature and strain rate on dynamic fracture toughness of steel." *Journal of the Society of Naval Architects of Japan* Vol. 158 (1985): pp. 619–629.

[27] Toyosada, Masahiro, Fujii, Eisuke, Nohara, Kazuhiro, Kawaguchi, Yoshiaki, Arimochi, Kazushige and Isaka, Kazumi. "The Effect of Strain Rate on Critical CTOD and J Integral." *Journal of the Society of Naval Architects of Japan* Vol. 1987 No. 161 (1987): pp. 343–356. DOI 10.2534/jjasnaoe1968.1987.343.

[28] Itabashi, Masaaki and Kawata, Kozo. "Carbon content effect on high-strain-rate tensile properties for carbon steels." *International Journal of Impact Engineering* Vol. 24 No. 2 (2000): pp. 117–131. DOI 10.1016/s0734-743x(99)00050-0.

[29] Choung, Joonmo, Nam, Woongshik and Lee, Jae-Yik. "Dynamic hardening behaviors of various marine structural steels considering dependencies on strain rate and temperature." *Marine Structures* Vol. 32 (2013): pp. 49–67. DOI 10.1016/j.marstruc.2013.02.001.

[30] Forni, Daniele, Chiaia, Bernardino and Cadoni, Ezio. "Strain rate behaviour in tension of S355 steel: Base for progressive collapse analysis." *Engineering Structures* Vol. 119 (2016): pp. 164–173. DOI 10.1016/j.engstruct.2016.04.013.

[31] Paik, Jeom Kee, Kim, Ki Jong, Lee, Jong Hwan, Jung, Bo Gyeong and Kim, Sang Jin. "Test database of the mechanical properties of mild, high-tensile and stainless steel and aluminium alloy associated with cold tem-

peratures and strain rates." *Ships and Offshore Structures* Vol. 12 No. sup1 (2017): pp. S230–S256. DOI 10.1080/17445302.2016.1262729.

[32] Chen, Junling, Shu, Wenya and Li, Jinwei. "Constitutive model of Q345 steel at different intermediate strain rates." *International Journal of Steel Structures* Vol. 17 No. 1 (2017): pp. 127–137. DOI 10.1007/s13296-016-0122-8.

[33] Bai, Yuanli and Wierzbicki, Tomasz. "Application of extended Mohr–Coulomb criterion to ductile fracture." *International Journal of Fracture* Vol. 161 No. 1 (2010): pp. 1–20. DOI 10.1007/s10704-009-9422-8.

[34] Anderson, Thomas L. *Fracture Mechanics: Fundamentals and Applications*, 4th ed. CRC Press, Boca Raton (2017). DOI 10.1201/9781315370293.

[35] Bao, Yingbin and Wierzbicki, Tomasz. "On the cut-off value of negative triaxiality for fracture." *Engineering Fracture Mechanics* Vol. 72 No. 7 (2005): pp. 1049–1069. DOI 10.1016/j.engfracmech.2004.07.011.

[36] CEN (European Committee for Standardization). *EN 10025-6 Hot rolled products of structural steels - Part 6: Technical delivery conditions for flat products of high yield strength structural steels in the quenched and tempered condition*. CEN, Brussels (2019).

[37] ASTM (American Society for Testing and Materials). *E1820 - 23b Standard Test Method for Measurement of Fracture Toughness*. ASTM, West Conshohocken (2023). DOI 10.1520/E1820-23B.

[38] IACS (International Association of Classification Societies). *IACS UR W Requirements concerning material and welding*. IACS (2023).

[39] ISO (International Organization for Standardization). *ISO 148-1 Metallic materials - Charpy pendulum impact test - Part 1: Test method*. ISO (2016).

[40] ISO (International Organization for Standardization). *ISO 14556 Metallic materials - Charpy V-notch pendulum impact test - Instrumented test method*. ISO, Geneva (2023).

[41] Needleman, Alan and Tvergaard, Viggo. "An analysis of ductile rupture in notched bars." *Journal of the Mechanics and Physics of Solids* Vol. 32 No. 6 (1984): pp. 461–490. DOI 10.1016/0022-5096(84)90031-0.

[42] Needleman, Alan. "Material rate dependence and mesh sensitivity in localization problems." *Computer Methods in Applied Mechanics and Engineering* Vol. 67 No. 1 (1988): pp. 69–85. DOI 10.1016/0045-7825(88)90069-2.

[43] de Borst, René, Crisfield, Mike A., Remmers, Joris J. C. and Verhoosel, Clemens V. *Nonlinear Finite Element Analysis of Solids and Structures*, 2nd ed. John Wiley & Sons Ltd, West Sussex, United Kingdom (2012).

[44] Considère, Armand. "Mémoire sur l'emploi du fer et de l'acier." *Annales des Ponts et Chaussées* Vol. 9 (1885): pp. 574–775.

[45] Xue, Liang and Wierzbicki, Tomasz. "Ductile fracture initiation and propagation modeling using damage plasticity theory." *Engineering Fracture Mechanics* Vol. 75 No. 11 (2008): pp. 3276–3293. DOI 10.1016/j.engfracmech.2007.08.012.

[46] Xue, Liang. "Stress based fracture envelope for damage plastic solids." *Engineering Fracture Mechanics* Vol. 76 No. 3 (2009): pp. 419–438. DOI 10.1016/j.engfracmech.2008.11.010.

